Young's Modulus of Tungsten Infiltrated Carbon Nanotube Structures

Richard Cass

A senior thesis submitted to the faculty of

Brigham Young University

In partial fulfillment of the requirements for the degree of

Bachelor of Science

Richard Vanfleet, Advisor

Department of Physics and Astronomy

Brigham Young University

21 April 2021

Copyright © 2021, Richard Cass

All Rights Reserved

ABSTRACT

Mechanical Properties of Tungsten Infiltrated Carbon Nanotube Structures

Richard Cass

Department of Physics and Astronomy

Bachelor of Science

Carbon Nanotube Templated Microfabrication (CNT-M) processes use nanotube forest growth from a 2D pattern to form 3D structures. The resulting structure is then infiltrated with a second material such as carbon or tungsten to form the final device. Materials properties of these structures with different infiltration materials and varying degrees of infiltration are of interest. We have used force-displacement data (in fixed-free and 3-point bending configurations) to determine the Young's modulus of tungsten infiltrated CNT structures (W-CNT's). Via this method we found the Young's modulus of (W-CNT's) to be 8.7 ± 5.2 GPa. However, in the case of the tungsten infiltration processes and typical test beams (~250 μm in width), the infiltration was not sufficiently uniform for high confidence results. Smaller beams (< 50 μm width) are difficult to handle using the conventional 3-point bending processes. We report resonance frequency testing, using a Laser Doppler Vibrometer (LDV), of thin CNT-M cantilevers to find the Young's modulus of these CNT structures when infiltrated with tungsten. We found the Young's modulus of W-CNT's developed using our lab's process to be 8.9 ± 4.1 GPa.

Keywords: CNT, tungsten, MEMS, Young's modulus

Acknowledgements

I would like to acknowledge all those who helped and supported me through all this work. My advisors, Richard Vanfleet and Robert Davis, were the pillars of support and guidance I needed as I conducted the research and wrote my reports. Paul Minson and the BYU Electron Microscopy Facility were instrumental in obtaining the high-quality SEM images that helped me analyze the quality of my experiments and make the necessary adjustments. Brian Anderson and the BYU Acoustics Group allowed me to use the LDV system. My girlfriend, Amanda Galán, was a constant support through this all. Finally, I would like to thank the BYU College of Physical and Mathematical Sciences and the Physics Department for funding this project.

Table of Contents

Table of Figures viii

List of Tables x

Chapter 1: Introduction 1

1.1 Motivation 1
1.1.1 Carbon Nanotube Micro-Electrical-Mechanical Systems 1
1.1.2 Tungsten 2

1.2 Background, Previous Work at BYU 3

Chapter 2: Methods 4

2.1 CNT Sample Preparation 4
2.1.1 Sample Templating 4
2.1.2 Sample Growth 5

2.2 Sample Infiltration and Release 6
2.2.1 Ozone Treatment 6
2.2.2 Tungsten Infiltration 6

2.3 Three-Point Bending Approach 8
2.3.1 Three-Point Bending Theory 8
2.3.2 Three-Point Bending Application 9

2.4 Modal Frequency Analysis Approach 13
2.4.1 Modal Frequency Analysis Theory 13
2.4.2 Laser Doppler Vibrometry 14
2.4.3 Modal Frequency Analysis Application 15

2.5 Error Analysis 17

Chapter 3: Results 18

3.1 Three-Point Bending Results 18

3.2 Modal Frequency Analysis Results 19

3.3 Uncertainty Results 22

3.4 Conclusions 22

3.5 Future Work 23

Index 24

Works Cited 25

Table of Figures

Figure 1: A cell grabber created using the CNT-M technique employed by our research group. Note the micro-scale of this MEMS example [7]. 2

Figure 2: A representation of the photolithography process used to template the CNT growth. .. 5

Figure 3: A depiction of the growth of carbon nanotubes. The substrate is a silicon wafer coated with alumina. The nanotubes grow in the pattern of, and directly from, the 2D patterned iron..... 6

Figure 4: Representation of the reaction that occurs during a tungsten ALD cycle. 7

Figure 5: A representation of a three-point bending experiment where the sample being tested is the rectangle spanned across the triangles. 9

Figure 6: Mini instron setup for three-point bending tests [6]..... 10

Figure 7: The force displacement curves for one batch of 10 beams under the same growth and infiltration conditions. 10

Figure 8: SEM image of the cross section of a tungsten infiltrated CNT beam (75 ALD cycles). The image was taken in high contrast to highlight the nonuniform tungsten infiltration. Lighter color indicates greater tungsten concentration. The banding on infiltration is shown in the red boxes. 11

Figure 9: Basic schematic of a laser doppler vibrometer, by Laderaranch - Own work, Public Domain, https://commons.wikimedia.org/w/index.php?curid=4846897..... 15

Figure 10: The mask pattern for the samples used in one of the tests. The red areas are where CNT's would grow. 16

Figure 11: A) Isometric view of the animation of the first mode of vibration of a beam approximately 1mm long and 200 µm wide. B) Side view of the animation of the second mode of vibration of the same beam. C) Side view of the animation of the third mode of vibration of

the same beam. Comparing these modal shapes to the standard expected mode shapes confirms that these are the afore identified modes..... 19

Figure 12: Cross sections of two beams fabricated for use in modal frequency analysis testing. a) A beam that grew and released properly, no structural failures. b) A beam that shows structural fracturing after release from substrate. 20

List of Tables

Table 1: Young's modulus calculation data under homogeneous beam assumption 18

Table 2: Young's modulus calculation data under the tungsten shell assumption 19

Table 3: Young's modulus calculation data using the modal frequency analysis approach. The column “Clean Data?” indicated whether or not a beam was included in the analysis, with “N” meaning the beam had structural fracturing as shown in Figure 12. 21

Chapter 1: Introduction

1.1 Motivation

1.1.1 Carbon Nanotube Micro-Electrical-Mechanical Systems

Micro-electro-mechanical systems (MEMS) are small systems, typically in the range of micrometers, that serve either an electrical or mechanical purpose. A growing industry, MEMS take a continuously increasing variety of forms, from an electrically activated mechanical actuator, to a cell grabber (shown in Figure 1), to a micro gas sensor, etc. The leading material for producing MEMS is silicon due to it experiencing less structural fatigue from motion compared to other materials, making it highly reliable in the long run [1]. However, silicon MEMS consists of complex crystalline structure, and is quite expensive to produce [1]. We hope to overcome these disadvantages by using carbon nanotubes (CNT's) and tungsten to produce MEMS which will be cheaper and have tunable materials properties which will make them useful in a variety of circumstances.

In our research group we employ the method of Carbon Nanotube Templated Manufacturing (CNT-M) to make MEMS [2]. In this process we use photolithography to lay out a 2D template of the MEMS we wish to create [3]. We then process the wafer and grow a carbon nanotube forest in the pattern we templated on the wafer. We fill this forest with a material that we choose to give the whole structure specific material properties [4]. Previous students in our research group have extensively studied carbon infiltrated carbon nanotube structures (CI-CNT's) [5, 6]. In this project we studied the materials properties, specifically the Young's modulus, of tungsten infiltrated carbon nanotubes structures (W-CNT's).

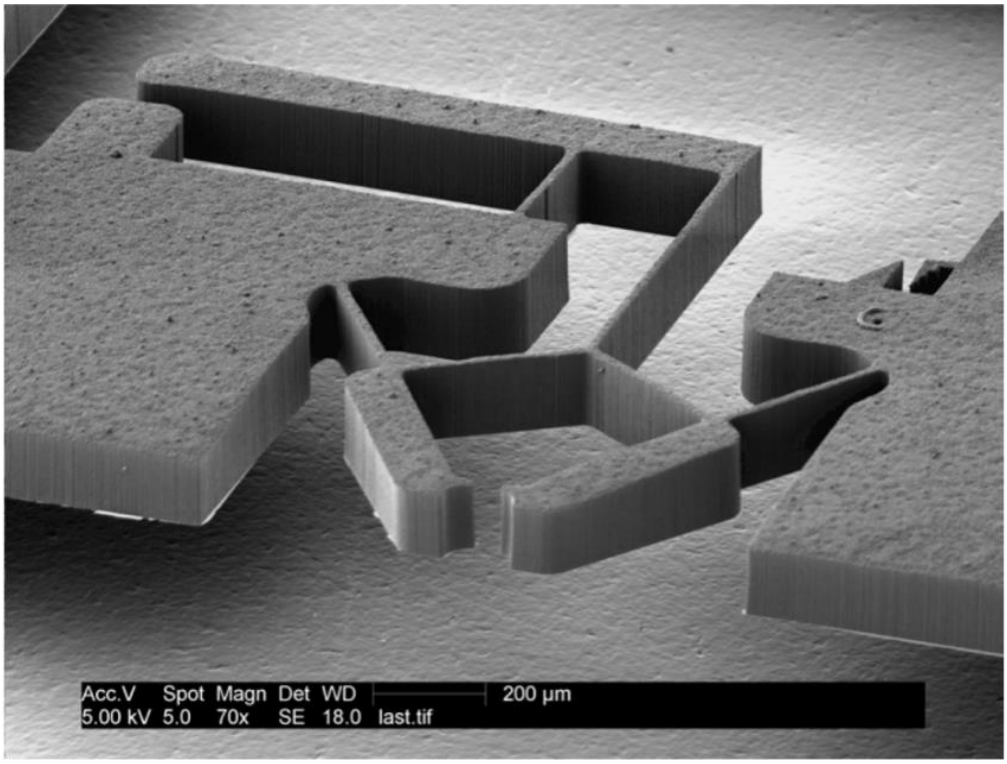


Figure 1: A cell grabber created using the CNT-M technique employed by our research group. Note the micro-scale of this MEMS example [7].

1.1.2 Tungsten

In my research group, we are specifically interested in studying CNT structures that have been infiltrated with tungsten [4]. Due to its high Z-value (Z = 74) and recent advancements in the tungsten machining process, tungsten is commonly used for collimators in x-ray machines [8] . However, these are made via a relatively difficult additive manufacturing process which limits their aspect ratio (typically about 4:1 [9]) and minimum size. Using W-CNT's, in my research group we can produce samples that are smaller, and with a higher aspect ratio (at least 9:1) which would allow for smaller and cheaper x-ray collimators. In order to put these samples in use, we want to know the materials properties of the samples to know how to handle, process, ship, and implement them in current systems.

One of the most important material properties to study is the Young's modulus which is a measure of how the force applied to the material is related to the strain in the material. It is effectively a measure of the "flexibility" of the material [10]. By finding the Young's modulus of the W-CNT's we will know how the samples need to be handled and packaged for use in x-ray machines. Furthermore, we will be able to identify other applications where W-CNT's may prove useful.

1.2 Background, Previous Work at BYU

Previously at BYU, we have performed many studies on CNT structures in various situations. We have extensively studied the CNT generation process [2, 5, 6] using our standard procedure and can reliably generate CNT structures. We have also studied the material properties of carbon infiltrated CNT structures (CI-CNT's) using methods such as three-point bending [5, 6] and dual deflection [2]. We have performed studies attempting to optimize the tungsten deposition process, though there are still some shortcomings in this process which will be discussed later in this paper. For this experiment I will follow our research group's standard sample generation process and standard tungsten deposition process. I will also use the same three-point bending approach to evaluate the Young's modulus as used in the previous studies.

Chapter 2: Methods

In this chapter I discuss the methods used in this experiment. Specifically, I will cover the sample generation process, the testing process, and the equations used to calculate the Young's modulus.

2.1 CNT Sample Preparation

2.1.1 Sample Templating

The start of the sample generation process is photolithography. Through the process of photolithography, we layout a 2D template of where the CNT's will grow. As shown in Figure 2, we coat the top surface of our sample wafer with a layer of positive photoresist, AZ3330, then expose the wafer to UV light through a mask with our desired pattern. This mask shadows the 2D pattern of where we want CNT's to grow on the wafer. We then immerse the wafer in a developer which removes the unexposed photoresist (the photoresist that was in the shadow of the mask) leaving holes in the photoresist where we want CNT growth.

Once the photoresist pattern has been laid out on the wafer, we coat the wafer with iron (4 nm thick) via a thermal deposition process. The iron coats the entire wafer, both where there is and is not photoresist. We immerse the wafer in an organic solvent (NMP) which removes the photoresist still on the wafer. As shown in the bottom right image of Figure 2, because removing the photoresist also removes the iron deposited on top of it, we are now left with a 2D template of iron in the pattern of how we want the CNT's to grow.

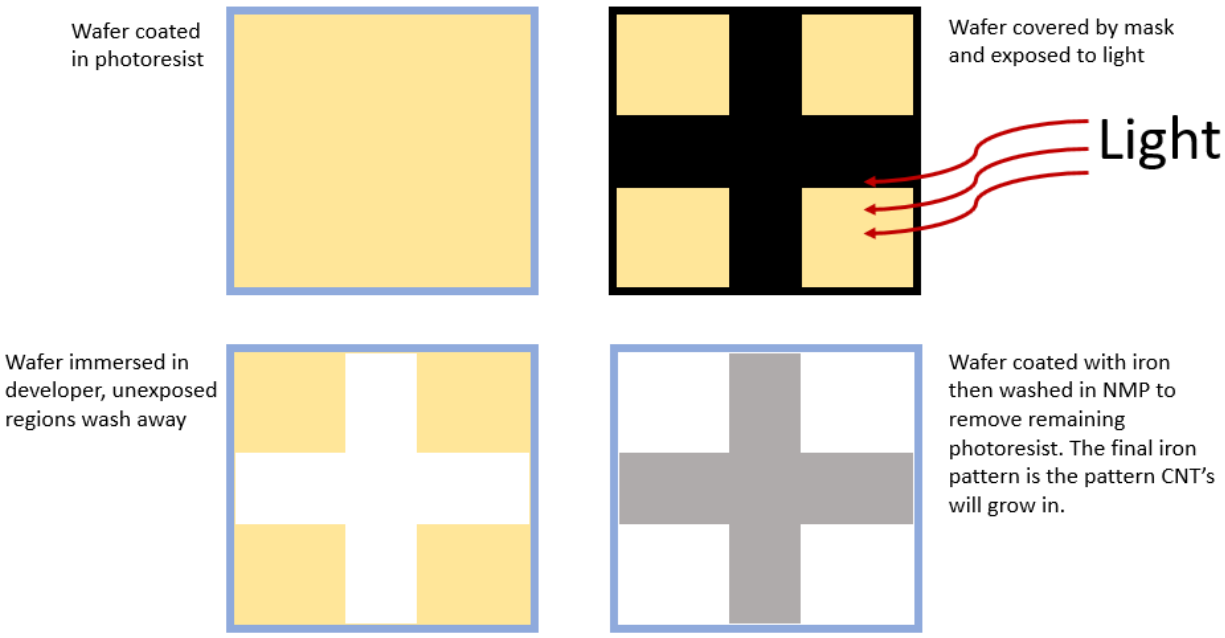


Figure 2: A representation of the photolithography process used to template the CNT growth.

2.1.2 Sample Growth

Once the iron has been templated on the wafer, we grow the carbon nanotubes through a standard chemical vapor deposition (CVD) process [2, 11]. After making the 2D iron template on the wafer, we put our wafer sample in a furnace and flow ethylene (C_2H_4) and hydrogen (H_2) at 750^o Celsius. As shown in Figure 3, the carbon nanotubes grow directly from the iron. We leave the sample in the furnace for a set amount of time to allow the sample to grow to about 200 µm (shorter or taller is possible based on the time), then remove it from the furnace. The sample is then ready for use or for further treatment, depending on the intended application.

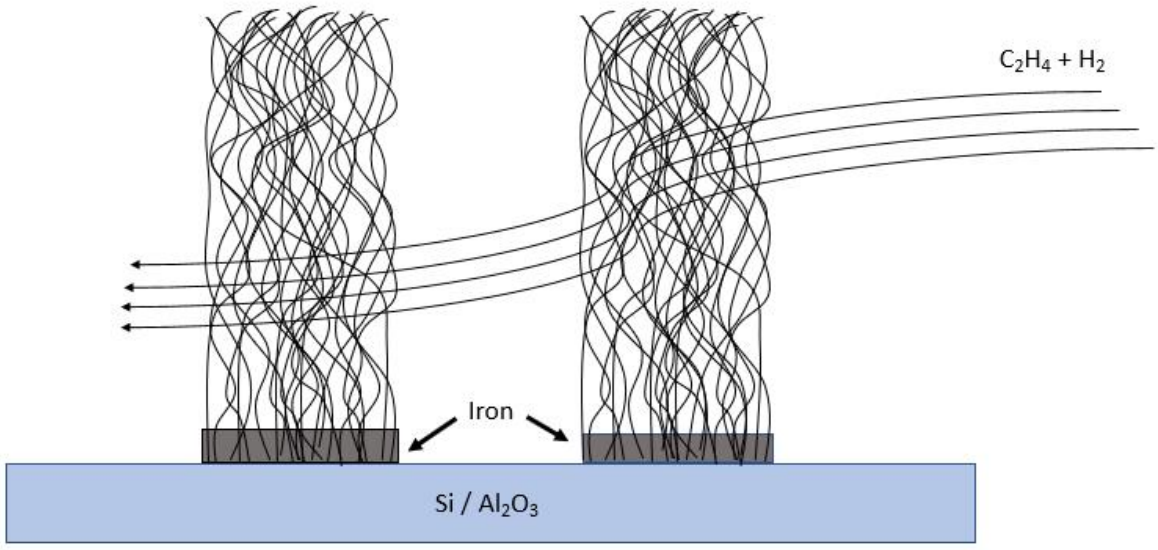


Figure 3: A depiction of the growth of carbon nanotubes. The substrate is a silicon wafer coated with alumina. The nanotubes grow in the pattern of, and directly from, the 2D patterned iron.

2.2 Sample Infiltration and Release

2.2.1 Ozone Treatment

Once the sample is grown, we prepare it for tungsten infiltration by first treating it with ozone. This treatment increases the number of nucleation sites where tungsten clusters will begin to grow on the sample, enabling more full and rapid coverage of the carbon nanotubes with tungsten [4]. In this process, the sample is placed in the output stream of an ozone generator operating with a regulated input pressure of 20 psi, a flow rate of 7 SCFH, and an ozone output of 45%. The sample is left in the stream for 30 minutes to ensure enough nucleation sites are created [4].

2.2.2 Tungsten Infiltration

Once the sample has been treated with ozone, we put the sample in a low-pressure chamber and perform the tungsten infiltration process. Atomic layer deposition (ALD) is a process in which a sample is exposed to an alternating series of gasses, where each cycle of

gasses deposits a single atomic layer of the desired material. The tungsten ALD process we use utilizes the gasses silane (SiH_4) and tungsten hexaflouride (WF_6), as shown in Figure 4. This reaction occurs by the following method [12]:

$$SiH_4 + WF_6 \rightarrow W + a\ Si H_x F_y + b\ H_2 \quad (1)$$

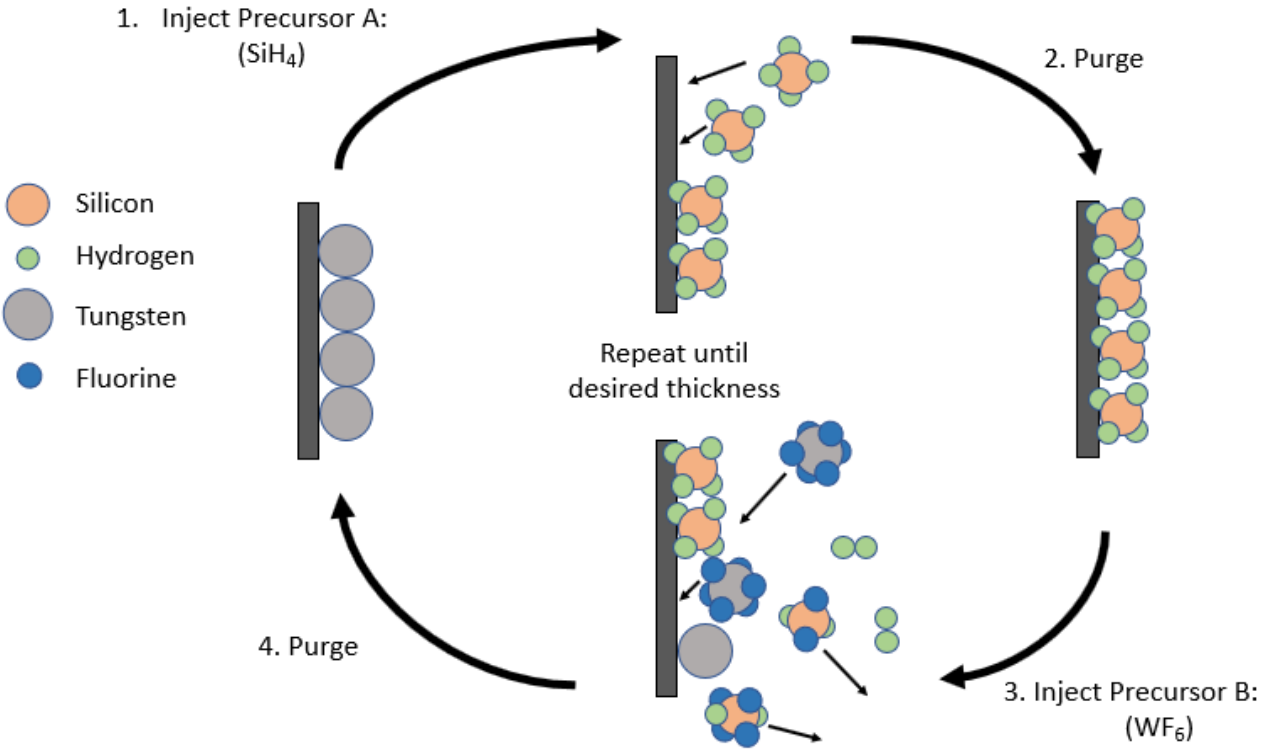


Figure 4: Representation of the reaction that occurs during a tungsten ALD cycle.

As demonstrated in Figure 4, to begin the tungsten ALD process the chamber is injected with precursor A, silane. The silane (SiH_4) is permitted to permeate through the chamber and sample for a set amount of time (the dwell time), during which time the silane will react with the nucleation site at the surface of the nanotubes and coat the nanotubes. After the dwell time is completed, the chamber is purged with argon to dilute out the excess silane, then pumped down to remove the excess reagent. Once the chamber is pumped, the second precursor, WF_6, is injected into the chamber. The tungsten hexafluoride is left to dwell in the chamber for a certain amount of time (the second dwell time), during which time it reacts with the silane, coating the

sample in tungsten and generating the gaseous products. Following the dwell time, the chamber is again purged and pumped, removing any excess WF_6 and the generated products. This single cycle has laid down a layer of tungsten on the carbon nanotubes. This cycle is repeated a certain number of times until the desired deposition layer thickness is deposited, with each layer depositing another layer of tungsten. For our samples we performed 75 deposition cycles.

Because of the nucleation sites, the tungsten will stick to the CNT's while the other products will be pumped out of the chamber by the system. Proper care must be taken to ensure that the excess gaseous products are properly removed from the system to prevent health hazards and sample contamination in later cycles.

2.3 Three-Point Bending Approach

2.3.1 Three-Point Bending Theory

Three-point bending is a standard method for determining various material properties in samples. The sample, typically a rectangular beam, is supported on both ends while another source applies force in the center of the beam. As the source applies force in the center of the beam, there is a sensor that measures the force being applied versus the distance the source has travelled. We can calculate the Young's modulus, E, of the sample from the slope of the force-displacement curves using the following equation (assuming a uniform material, rectangular cross section) [13],

$$E = \frac{L^3 m}{4bd^3} \tag{2}$$

Where E is the Young's modulus of the sample, L is the span over which the beam is supported as shown in Figure 5, m is the gradient (slope in the 2D case) of the force-deflection curves such as in Figure 7, b is the width of the beam, and d is the thickness of the beam, shown in Figure 5.

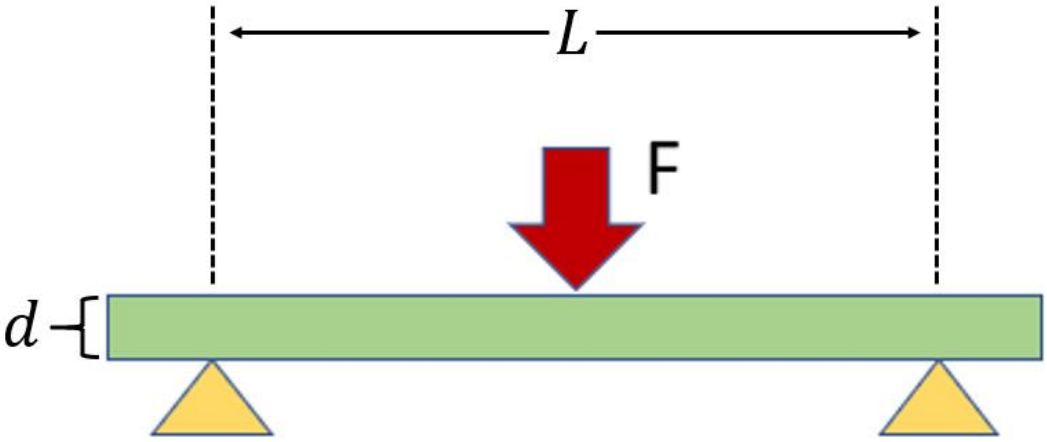


Figure 5: A representation of a three-point bending experiment where the sample being tested is the rectangle spanned across the triangles.

2.3.2 Three-Point Bending Application

For this method of testing, we patterned our CNT structures to be simple rectangular prisms, 6 mm long and about 300 µm tall. We tested three different beam widths: 150 µm, 250 µm, and 300 µm. Once we made our beams, we used a mini instron machine to perform the three-point bending tests on the beams. We bridged the beam across a gap of three millimeters and applied a downward force in the middle of the beam with a razorblade as shown in Figure 6. The razorblade was mounted on a force sensor which measured how much force was being applied to the beam. As the mini instron descended, it measured the distance it had travelled. Thus, as shown in Figure 7, we were able to collect both force and displacement measurements for our experiment.

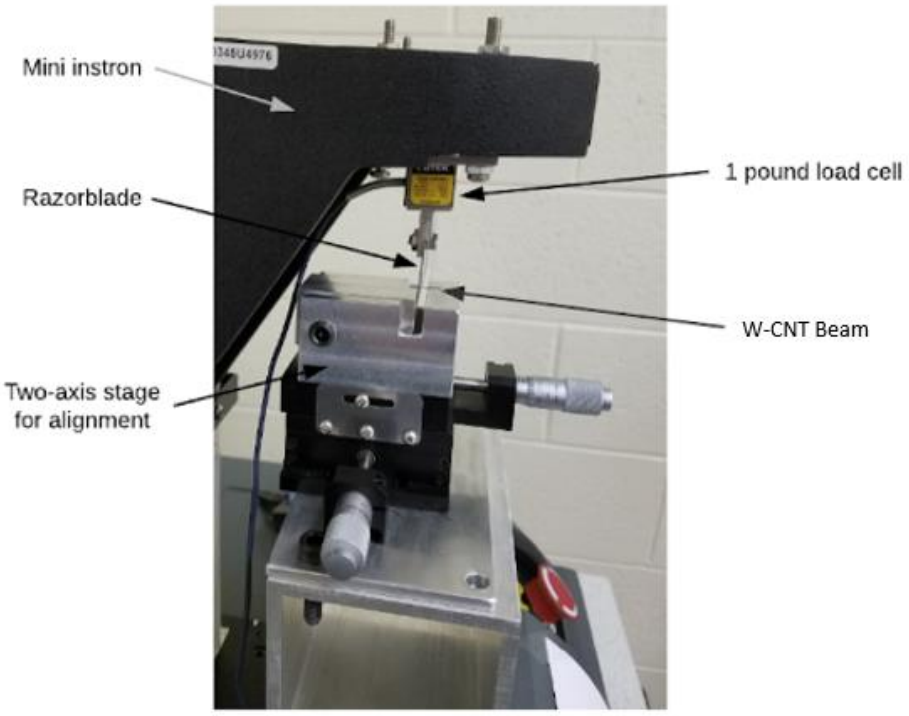


Figure 6: Mini instron setup for three-point bending tests [6]

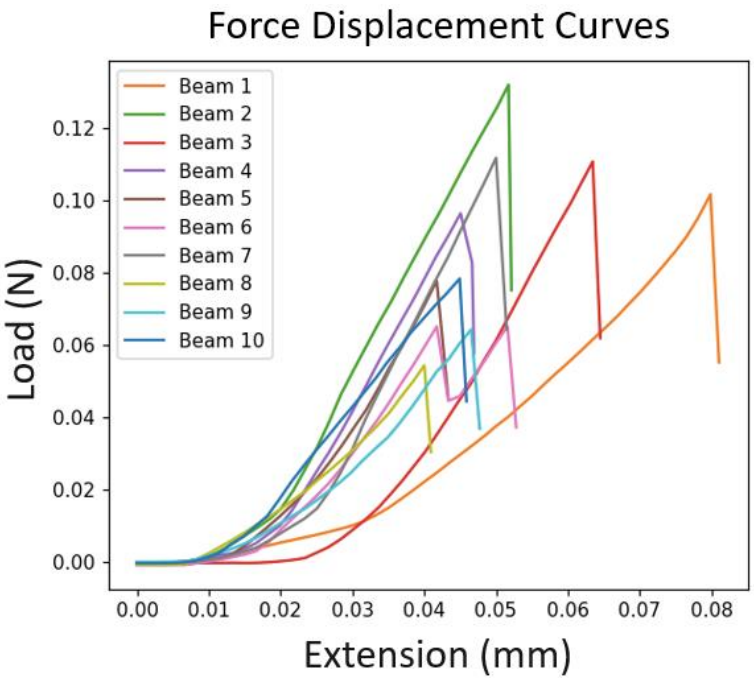


Figure 7: The force displacement curves for one batch of 10 beams under the same growth and infiltration conditions.

From graphical outputs like the one above, and knowing the beam dimensions, we were able to calculate the Young's moduli of our samples using Equation (2). However, these calculations operate under the assumption that the beam is one uniform material with a rectangular cross section. As seen in SEM images of the cross section of the beams as shown in Figure 8, the tungsten deposition forms bands in the cross section of the beam. In this figure, the brighter bands show a higher concentration of tungsten while darker areas represent less tungsten. Thus, we concluded that the beams were not fully infiltrated with tungsten.

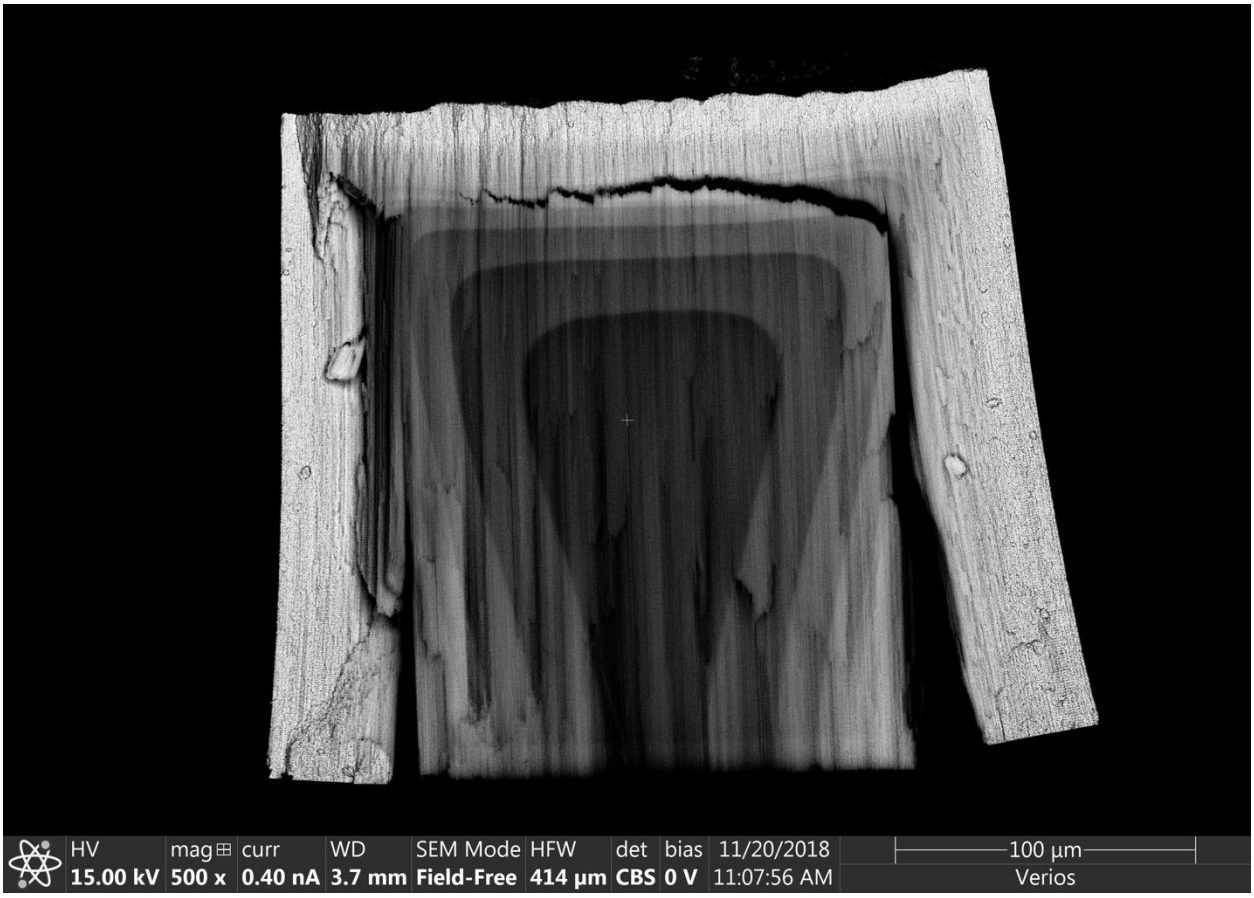


Figure 8: SEM image of the cross section of a tungsten infiltrated CNT beam (75 ALD cycles). The image was taken in high contrast to highlight the nonuniform tungsten infiltration. Lighter color indicates greater tungsten concentration.

These bands develop due to a combination of the tangled scaffolding the carbon nanotubes form, and the nature of the W-ALD process in general. Because the nanotubes are so tangled, it takes more time for particles during the ALD process to find their way into the depths of the sample due to slower diffusion of the gasses [14]. Another feature that limits the deposition in later cycles is that as more tungsten is developed and forms progressively larger beads, there is more surface area for the silane to react with, slowing the diffusion even further.

Examining the SEM images, we made the assumption that the tungsten is deposited uniformly around the edge of the cross section of the beam in an "n" shape. Under this assumption, and using standard material analysis approaches, we determined a modified equation to calculate the Young's modulus of the beams in which we only include the "n" shape of material and ignore the interior material [15]. Equation (3) is the equation used to calculate the Young's modulus, E. This equation depends on the moment of inertia of the beam, I, as given in Equation (4). There is a term in Equation (4) that is repeated a few times, $\bar{y}$, so for simplicity's sake this term is shown in Equation (5).

$$E = \frac{L^3 m}{48 I} \tag{3}$$

$$I = \frac{t\,h^3}{6} + \frac{t^3(b-2t)}{12} + 2h\,t\left(\frac{h}{2} - \bar{y}\right)^2 + t(b-2t)\left(h - \frac{t}{2} - \bar{y}\right)^2 \tag{4}$$

$$\bar{y} = \frac{h^2 + (b-2t)\left(h - \frac{t}{2}\right)}{2h + b - 2t} \tag{5}$$

In these equations, L is the length of the span over which the beam is bridged, m is the gradient (slope in the 2D case) of the force-deflection curves, t is the thickness of the uniform tungsten shell, b is the width of the beam, and h is the height of the beam in the direction of bending.

Examining the SEM images of the beams, we estimated the thickness of the uniform tungsten band, t to be 15 µm. With this assumption we were able to continue with our calculations. However, given that the estimation for the shell thickness is a very subjective measure, an improved approach would be to make and measure thinner beams that would have uniform tungsten infiltration throughout the beam. However, these thinner beams would be too thin to be handled manually for use in the three-point bending test, so we determined we needed another method to calculate the Young's modulus.

2.4 Modal Frequency Analysis Approach

2.4.1 Modal Frequency Analysis Theory

Modal frequency analysis is another standard method for determining the Young's modulus of a material. Knowing the dimensions and density of a cantilever beam, by vibrating the beam and examining the modal frequencies of vibrations, one can calculate the Young's modulus of the beam. Following the equations given in "Understanding Acoustics" [16], we solved a differential equation relating the Young's modulus to various physical properties of a cantilever. Once the general solution was obtained, the boundary conditions gave us the specific solutions for our setup. As part of this solution, the following periodic transcendental equation is solved numerically [16]:

$$coth^2(x) = tan^2(x) \tag{6}$$

The solutions of Equation (6) are scaling factors for the Young's modulus equation in Equation (7). In the case of our setup (a cantilever beam that is fixed at one end and free at the other) the equation to find the Young's modulus, E, is the following [16]:

$$E = 12\rho \left[\frac{8 \cdot f_n \cdot L^2}{\pi \cdot {\alpha_n}^2 \cdot H} \right]^2 \tag{7}$$

where ρ is the density (found by measuring the mass of one sample and calculating the volume of the sample using the sample mask dimensions and measured height, then dividing the mass by the volume), f_n is the frequency of the n^{th} longitudinal vibrational mode, L is the length of beam, H is the height of beam, and α_n is the n^{th} term of solutions to the transcendental equation mentioned above, $(1.194,\ 2.9884,\ 5.0005,\ 7,\ 9,\ 11\ \ldots\ )$.

2.4.2 Laser Doppler Vibrometry

In order to measure the vibrations of our cantilever samples we used a laser doppler vibrometer (LDV). An LDV uses the principle of the doppler effect to measure the velocity of an object. The general schematic of an LDV is shown in Figure 9: it begins with a laser beam that gets split into a reference beam and a scanning beam. The scanning beam is sent through a Bragg cell which adds a known frequency shift (Bragg frequency) to the signal [17]. When the signal beam reaches the object, it will experience a frequency shift due to the object's vibration. The shifted signal beam is then recombined with the original reference beam. The two combined beams are now different frequencies and thus cause beating in the response picked up by the detector. This beating occurs at the Bragg frequency plus or minus the doppler shift due to the vibration of the sample (a positive shift when the sample is moving towards the laser, and a negative shift when the sample moves away). From the beating pattern the LDV can calculate the velocity of the sample at a certain time. When the sample is driven through a frequency sweep, the LDV can perform a time-based Fourier transform to map the response to the driving frequency.

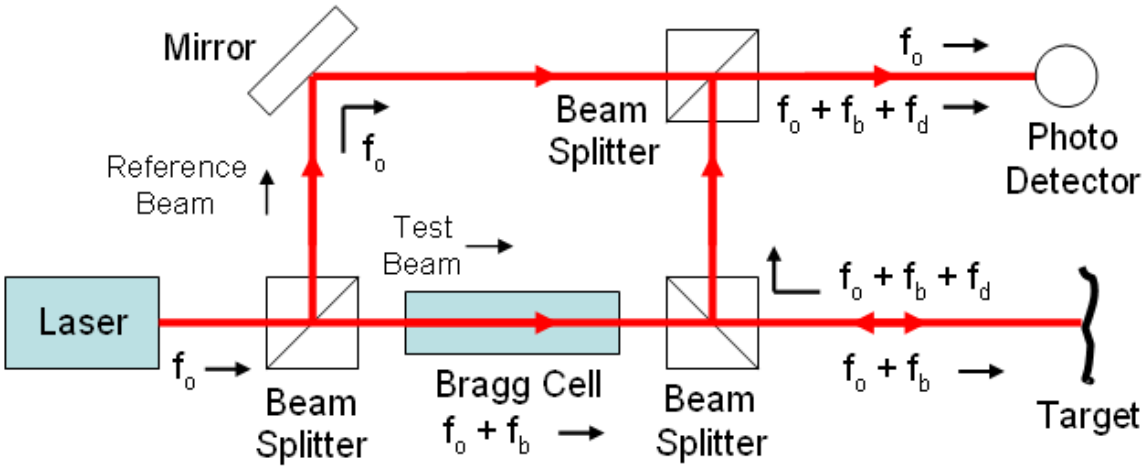


Figure 9: Basic schematic of a laser doppler vibrometer, by Laderaranch - Own work, Public Domain, https://commons.wikimedia.org/w/index.php?curid=4846897

2.4.3 Modal Frequency Analysis Application

To allow for smaller beam widths thus more uniform infiltration, we designed a new sample pattern as shown in Figure 10. This mask allows us to generate thinner beams while still being able to handle the sample. It also allows us to orient the sample to achieve optimal signal from the cantilever vibrations.

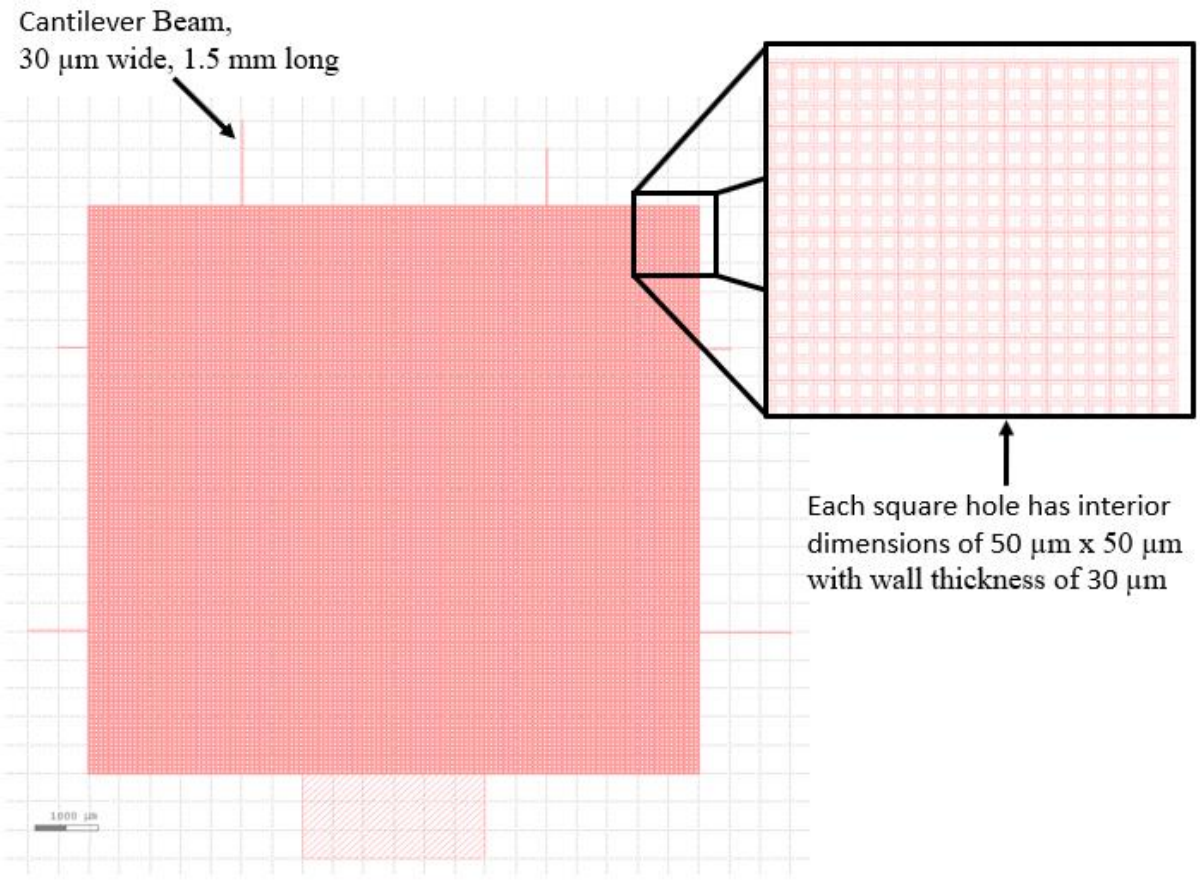


Figure 10: The mask pattern for the samples used in one of the tests. The red areas are where CNT's would grow.

For our experiment we had the LDV measure the vibrations of the cantilever beam over the length of the beam. The cantilevers were vibrated with a piezoelectric transducer that was driven through a sweep of frequencies. The beam was scanned by the LDV over a grid of points along the cantilever, where the driving frequency sweep was repeated for each scan point. In this way we were able to measure the response of the whole beam in terms of applied frequency. From the generated frequency vs velocity plots, we are able to select a certain frequency and the LDV will generate a 3D animation of the motion of the beam at that applied frequency. Using these animations, we identified which response peaks were modal responses (they look like the typical cantilever mode shapes) and using Equation (7), calculated the Young's modulus of the beams.

2.5 Error Analysis

In our testing we expect there to be sample-to-sample variation. This variation could come from a wide variety of sources, be it the growth process, the infiltration process, or how the sample is clamped during testing. We also expect there to be measurement error from the LDV system, as well as error in the measurement of the beam dimensions. I will account for these errors using standard uncertainty techniques and determine whether the majority of error is contained in sample-to-sample variation or measurement error.

Chapter 3: Results

3.1 Three-Point Bending Results

Using the three-point bending setup shown in Figure 6, we tested a total of 116 W-CNT beams and performed the homogenous beam assumption analysis on all of them. However, due to being unable to examine some of the samples under the SEM and estimate the tungsten shell thickness, we performed the tungsten shell analysis on only 84 beams. Under the assumption that the beams are infiltrated uniformly with tungsten (see Table 1), and using Equation (3), we found the Young's modulus of the W-CNT's to be 3.1 ± 2.6 GPa. Under the assumption that the infiltrated beams are effectively tungsten shells (see Table 2), and using Equation (4), we found the Young's modulus of the W-CNT's to be 8.7 ± 5.2 GPa. The uncertainty in each analysis is the standard deviation of the results.

Homogeneous Beam Analysis Young's Modulus Data

Beams 1-20		Beams 21-40		Beams 41-60		Beams 61-80		Beams 81-100		Beams 100-116	
Beam	**E (GPa)**	**Beam**	**E (GPa)**	**Beam**	**E (GPa)**	**Beam**	**E (GPa)**	**Beam**	**E (GPa)**	**Beam**	**E (GPa)**
1	2.02914	21	1.94788	41	2.6534	61	7.90309	81	3.39161	101	2.00309
2	3.10434	22	1.61864	42	1.19532	62	4.00581	82	2.46193	102	1.87387
3	2.28996	23	1.6504	43	1.94788	63	8.46989	83	1.21282	103	2.02914
4	1.19532	24	1.22084	44	1.61864	64	11.4456	84	2.60148	104	3.10434
5	1.94788	25	1.22084	45	1.6504	65	10.2693	85	1.90064	105	2.28996
6	1.61864	26	1.37651	46	1.22084	66	11.5268	86	2.02914	106	1.63872
7	1.6504	27	1.37651	47	1.22084	67	7.7864	87	3.10434	107	1.66336
8	1.22084	28	1.19532	48	1.37651	68	7.40139	88	2.28996	108	2.54474
9	1.22084	29	1.94788	49	9.59989	69	12.6135	89	1.63872	109	1.87716
10	1.37651	30	1.61864	50	8.13221	70	5.30847	90	1.66336	110	3.32419
11	1.37651	31	1.6504	51	3.65919	71	5.53291	91	2.54474	111	3.39161
12	1.25589	32	1.22084	52	6.73728	72	7.91117	92	1.87716	112	2.46193
13	1.80929	33	1.22084	53	7.06419	73	2.02914	93	3.32419	113	1.21282
14	2.71606	34	1.37651	54	0.16584	74	3.10434	94	3.39161	114	2.60148
15	3.1506	35	1.37651	55	5.62023	75	2.28996	95	2.46193	115	1.90064
16	2.84331	36	1.25589	56	7.35039	76	1.63872	96	1.21282	116	1.90064
17	2.6534	37	1.80929	57	7.4478	77	1.66336	97	2.60148		
18	1.86371	38	2.71606	58	4.77733	78	2.54474	98	1.90064		
19	1.304	39	3.1506	59	7.79736	79	1.87716	99	1.90064		
20	1.19532	40	2.84331	60	8.45604	80	3.32419	100	1.71661		

Table 1: Young's modulus calculation data under homogeneous beam assumption

Tungsten Shell Analysis Young's Modulus Data

Beams 1-15		Beams 16-30		Beams 31-45		Beams 46-60		Beams 61-75		Beams 76-84	
Beam	**E (GPa)**	**Beam**	**E (GPa)**	**Beam**	**E (GPa)**	**Beam**	**E (GPa)**	**Beam**	**E (GPa)**	**Beam**	**E (GPa)**
1	2.48767	16	3.80225	31	16.3402	46	6.12101	61	10.6227	76	13.885
2	2.31442	17	2.65416	32	0.35034	47	10.0168	62	13.959	77	6.25395
3	4.06311	18	2.48767	33	13.5892	48	9.17443	63	6.62719	78	10.1791
4	3.29458	19	2.31442	34	16.8379	49	7.53851	64	5.95389	79	16.2437
5	3.35922	20	4.06311	35	16.3786	50	11.9334	65	5.68749	80	11.9014
6	2.48489	21	3.29458	36	10.3652	51	10.6227	66	18.2319	81	9.78862
7	2.47881	22	3.35922	37	17.8994	52	7.48079	67	18.1278	82	10.165
8	2.66632	23	2.48489	38	17.2023	53	5.56804	68	13.8405	83	15.1979
9	2.84368	24	2.47881	39	19.2153	54	10.683	69	6.6952	84	11.2109
10	2.34135	25	2.66632	40	10.1165	55	5.3321	70	11.8447		
11	3.73467	26	6.90893	41	19.8254	56	6.12101	71	8.16547		
12	5.64654	27	20.4174	42	7.48079	57	10.0168	72	8.16547		
13	6.81151	28	17.6251	43	5.56804	58	9.17443	73	10.2776		
14	5.78728	29	8.49743	44	10.683	59	7.53851	74	10.9862		
15	4.89499	30	15.4659	45	5.3321	60	11.9334	75	10.2775		

Table 2: Young's modulus calculation data under the tungsten shell assumption

3.2 Modal Frequency Analysis Results

To determine which frequencies were modal frequencies for our cantilevers, we examined the 3D animations generated by the LDV at selected peaks in the frequency response plots. A still-shot of these animated plots is shown in Figure 11.

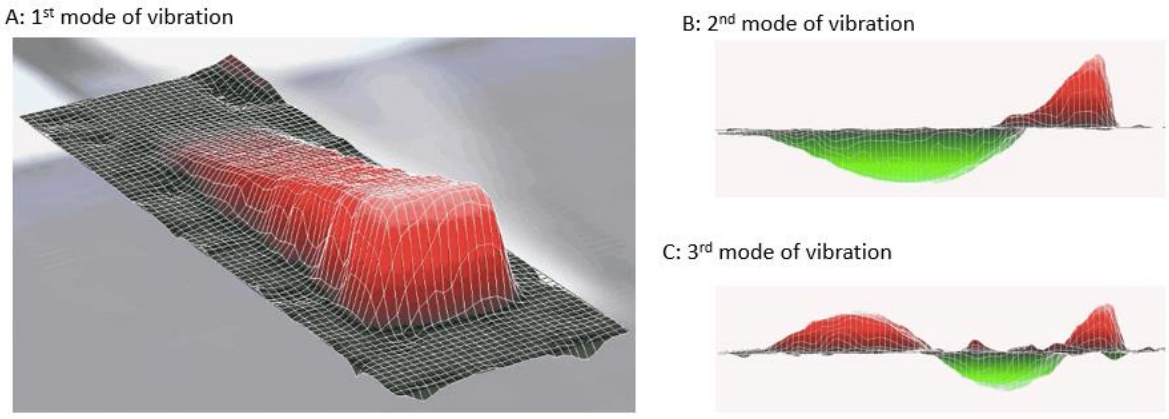


Figure 11: A) Isometric view of the animation of the first mode of vibration of a beam approximately 1mm long and 200 µm wide. B) Side view of the animation of the second mode of vibration of the same beam. C) Side view of the animation of the third mode of vibration of the same beam. Comparing these modal shapes to the standard expected mode shapes confirms that these are the aforementioned modes.

In applying the modal frequency analysis approach, one of the largest challenges was handling the beams. Due to the small size of the beams, they would often break or fracture. To ensure that these breakages did not affect the data, I examined the beams under an optical microscope. Under the microscope I measured the dimensions of the beam and visually inspected it to ensure there was not fracturing or warping in the beam as demonstrated in Figure 12. Any beams that exhibited warping or fracturing (or other anomalies) were excluded from the final calculations. With this restriction I included 67% of the original data in the final calculations. After applying Equation (5) to the data, I found the Young's modulus of the W-CNT's to be 8.9 ± 4.1 GPa, where the uncertainty is the standard deviation of the measurements. This value was calculated from the first modal frequency for each beam.

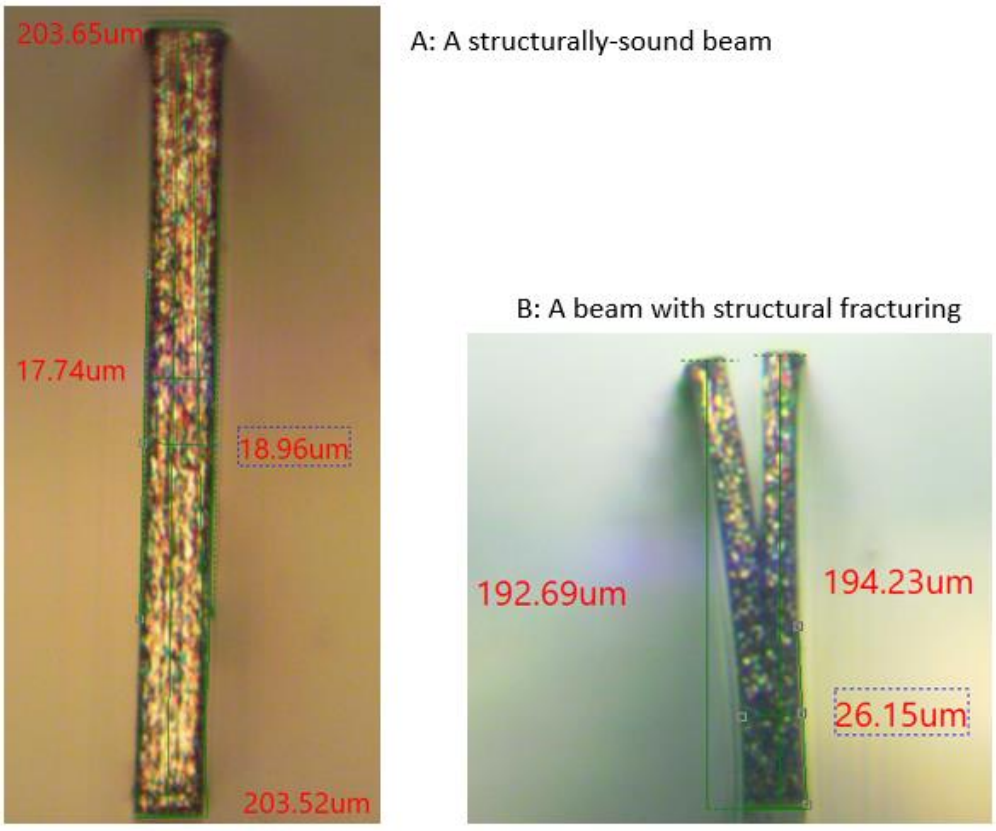


Figure 12: Cross sections of two beams fabricated for use in modal frequency analysis testing. a) A beam that grew and released properly, no structural failures. b) A beam that shows structural fracturing after release from substrate.

Modal Frequency Analysis Young's Modulus Data

Sample	Beam #	Clean Beam?	1st Mode E (GPa)
WRES 1	2	Y	5.753
WRES 2	5	N	1.181
WRES 3	6	N	1.872
WRES 3	5	Y	103.252
WRES 3	1	Y	3.789
WRES 4	3	N	110.505
WRES 4	2	N	0.0055
WRES 5	1	N	1.1296
WRES 5	2	Y	6.304
WRES 6	4	Y	5.173
WRES 6	3	Y	7.181
WRES 7	4	Y	6.953
WRES 7	2	Y	6.968
WRES 7	1	N	-
WRES 8	2	N	4.4195
WRES 8	4	N	7.047
WRES 8	5	Y	2.333
WRES 9	2	Y	7.032
WRES 9	1	N	0.831
WRES 10	5	N	4.701
WRES 10	2	Y	14.184
WRES 11	6	Y	18.398
WRES 11	5	Y	11.245
WRES 11	2	Y	11.282
WRES 12	2	Y	13.888
WRES 12	5	Y	12.153
WRES 13	3	Y	5.544
WRES 14	1	Y	9.693
WRES 15	2	Y	9.352
WRES 15	5	Y	11.563

Table 3: Young's modulus calculations using the modal frequency analysis approach. The column "Clean Data?" indicates whether or not a beam was included in the analysis, with "N" meaning the beam had structural fracturing, similar to Figure 12. These were all calculated using the first modal frequency for each beam with $\alpha = 1.194$.

One challenge we confronted in this analysis is that in practice, the modes were not distributed as predicted by the solutions to the transcendental equation shown in Equation (6) (1.194, 2.9884, 5.0005, 7, …). We found that the modes were distributed somewhere between what we would expect from fixed-free boundary conditions and hinged-free boundary conditions [16]. Because of this we are not certain on the exact value of the Young's modulus, but we are at least certain that we have the right order of magnitude.

3.3 Uncertainty Results

The two main sources of variability in the final calculations are the measurement error and the variability inherent in the sample generation process. I estimated the uncertainty in the dimension measurements to be 3.33% because we used a digital microscope to measure all the dimensions, and the uncertainty in the frequency measurement to be 1% due to the high precision of the LDV. Using the standard percent error propagation method, I found the overall percent uncertainty in the case of the modal frequency analysis approach to be 22%. Comparing this to the standard deviation of 46% from the modal frequency analysis calculation, we see that the variation in the sample is much larger than the variation due to the measurement technique. This is good because it means that our measurement method is not the limiting factor in the precision of our results. This means that the majority of the variation of the Young's modulus is due to the variation in the sample generation process.

3.4 Conclusions

We found the Young's modulus of W-CNT's grown using our lab's standard growth process and with 75 cycles of tungsten ALD to be be 8.7 ± 5.2 GPa with the three-point bending analysis under the tungsten shell assumption, and 8.9 ± 4.1 GPa with the modal frequency analysis approach. This value is also much lower than the Young's modulus of bulk tungsten which is about 340 GPa [18]. As can be seen, the value for the Young's modulus is very consistent between testing methods, providing more confidence to our calculation. With this value we can now determine how the samples would need to be packaged or handled for use inside x-ray collimators and how it could be used in other applications. Of note is that in work previously done at BYU, the Young's modulus of CI-CNT's was found to be 8.66 ± 3.1 GPa [5].

This is important because it means that our W-CNT samples maintain the Young's modulus of CI-CNT samples but have the added feature of being able to attenuate xrays. This is a very interesting effect and we're not sure what exactly causes the W-CNT structures to maintain the Young's modulus of CI-CNT's but still have x-ray attenuating ability.

3.5 Future Work

With the process developed during this project, future work includes conducting similar investigations with other infiltration metals. We already have a student performing studies with aluminum infiltration, and experiments with other metals would be excellent projects for other undergraduate students. Another study we can perform, which would be good for a graduate student perhaps, is attempting to identify the relationship between various sample generation processes and the Young's modulus. Through this study we would be able to identify what process we should use to obtain W-CNT beams with certain desired physical properties. We would then be able to generate samples to fulfill specific physical requirements. They would also be able to study the tungsten more closely and identify why the W-CNT's still have the Young's modulus of CI-CNT's. Another project that would help with the accuracy of our final calculations would be to perform finite element analysis on a model of a W-CNT sample to determine the proper way to model the boundary conditions for the cantilever beams.

Index

CNT
  Growth, 6
  Infiltration, 7
  Templating, 4
Laser Doppler Vibrometer (LDV), 15
MEMS
  CNT MEMS, 1
  Tungsten CNT MEMS, 2
Modal Frequency Analysis, 14
Three-Point Bending, 9
Tungsten ALD, Infiltration, 7

Works Cited

[1] Tilli, Markku. 2020. *Handbook of Silicon Based MEMS Materials and Technologies.* Elsevier Inc. doi:https://doi.org/10.1016/C2018-0-01845-9.

[2] Roberts, Spencer. 2020. "Mechanical Characterization of Carbon Nanotube based Neural Probes." Senior Thesis, Department of Physics and Astronomy, BYU.

[3] Sangwan, V.K. 2010. "Controlled Growth, Patterning and Placement of Carbon Nanotube Thin Films." *Solid-State Electronics* 54 (10): 1204-1210. doi:https://doi.org/10.1016/j.sse.2010.05.027.

[4] Hindsman-Curry, Eion. n.d. "Mechanical Property Measurements of Tungsten Infiltrated Carbon Nanotubes for High-Aspect-Ratio MEMS Fabrication." Report: BYU Physics REU Program, Physics and Astronomy, BYU.

[5] B. H. Hanna et al. 2014. "Mechanical Property Measurement of Carbon Infiltrated Carbon Nanotube Structures for Compliant Micromechanisms." *Journal of Microelectromechanical Systems* 23 (6): 1330-1339. doi:10.1109/JMEMS.2014.2312847.

[6] Sypherd, Shane. 2019. "Effects of Infiltration Temperature, Time, and Gas Flow Rate on Material Properties of Carbon Infiltrated Carbon Nanotubes." Thesis: Master of Science, Mechanical Engineering, BYU.

[7] Jensen, Brian. n.d. *Department of Mechanical Engineering, BYU.*

[8] Jeffery, Steve. 2019. *The Development of Tungsten Collimators MAy Advance Medical Imaging.* September 4. https://www.itnonline.com/article/development-tungsten-collimators-may-advance-medical-imaging.

[9] ScienceDirect. n.d. *Collimator.* https://www.sciencedirect.com/topics/engineering/collimator.

[10] Wikipedia. n.d. *Young's Modulus.* https://en.wikipedia.org/wiki/Young%27s_modulus.

[11] Brukh, Roman. 2006. "Mechanism of Carbon Nanotube Growth by CVD." *Chemical Physics Letters* 424 (1-3): 126-132. doi:https://doi.org/10.1016/j.cplett.2006.04.028.

[12] Chen, H. 1995. "Low pressure chemical vapor deposition of tungsten as an absorber for x-ray masks."

[13] Wikipedia. n.d. *Three-point Flexural Test.* https://en.wikipedia.org/wiki/Three-point_flexural_test.

[14] Kane, David. 2018. "Penetration Depth Variation in Atomic Layer Deposition on Multiwalled Carbon Nanotube Forests." Thesis: Master of Science, Physics and Astronomy, BYU.

[15] Moore, John. 2009. *Building Scientific Apparatus.* Vol. Building Scientific Apparatus. 2009 vols. Cambridge University Press. doi:https://doi.org/10.1017/CBO9780511609794.

[16] Garrett, Steven L. 2017. *Understanding Acoustics.* Springer International Publishing. doi: 10.1007/978-3-319-49978-9.

[17] Wikipedia. n.d. *Acousto-optic Modulator.* https://en.wikipedia.org/wiki/Acousto-optic_modulator.

[18] CiDRA. 2001. *Tungsten.* July 28. https://www.azom.com/properties.aspx?ArticleID=614.